

Interfacial Molecular Doping of Metal Halide Perovskites for Highly Efficient Solar Cells

Qi Jiang, Zhenyi Ni, Guiying Xu, Yun Lin, Peter N. Rudd, Rongming Xue, Yaowen Li,*
Yongfang Li, Yongli Gao, and Jinsong Huang*

Tailoring the doping of semiconductors in heterojunction solar cells shows tremendous success in enhancing the performance of many types of inorganic solar cells, while it is found challenging in perovskite solar cells because of the difficulty in doping perovskites in a controllable way. Here, a small molecule of 4,4',4'',4'''-(pyrazine-2,3,5,6-tetrayl) tetrakis (N,N-bis(4-methoxyphenyl) aniline) (PT-TPA) which can effectively p-dope the surface of $\text{FA}_x\text{MA}_{1-x}\text{PbI}_3$ (FA: $\text{HC}(\text{NH}_2)_2$; MA: CH_3NH_3) perovskite films is reported. The intermolecular charge transfer property of PT-TPA forms a stabilized resonance structure to accept electrons from perovskites. The doping effect increases perovskite dark conductivity and carrier concentration by up to 4737 times. Computation shows that electrons in the first two layers of octahedral cages in perovskites are transferred to PT-TPA. After applying PT-TPA into perovskite solar cells, the doping-induced band bending in perovskite effectively facilitates hole extraction to hole transport layer and expels electrons toward cathode side, which reduces the charge recombination there. The optimized devices demonstrate an increased photovoltage from 1.12 to 1.17 V and an efficiency of 23.4% from photocurrent scanning with a stabilized efficiency of 22.9%. The findings demonstrate that molecular doping is an effective route to control the interfacial charge recombination in perovskite solar cells which is in complimentary to broadly applied defect passivation techniques.

The enhancement of solar cell efficiency has been constantly pursued for reduced cost of solar energy systems. The power conversion efficiency (PCE) of perovskite solar cells (PSCs) has

surged from 3.8% to 25.2% in 10 years which has come out of global efforts in optimizing perovskites as well as charge transport layers.^[1] Tremendous efforts have been devoted to optimizing bandgap, improving crystallinity, controlling stoichiometry, and passivating defects of perovskite layer.^[2–4] Among them defect passivation has received tremendous attentions, which has been confirmed as an effective approach to reduce nonradiative charge recombination at interfaces as well as to stabilize the perovskite surfaces and bulk structure.^[4,5]


Selective doping of the interfacial layer(s) has been generally applied in silicon or other thin film photovoltaic technologies to enhance charge extraction and reduce recombination at the interfaces.^[6] To achieve this, precise doping manipulation is needed to selectively dope certain layers or regions, which is however challenging for metal halide perovskites (MHPs) due to the difficulty in intentionally doping MHPs. Nevertheless MHPs show self-doping behavior of both weakly p-type or n-type caused by defects.^[7,8] First-

principle computation predicted that $\text{CH}_3\text{NH}_3\text{PbI}_3$ can exhibit either p-type or n-type doping depending on the growth conditions,^[7] which has been experimentally confirmed by us in $\text{CH}_3\text{NH}_3\text{PbI}_3$ films fabricated from MAI-rich or PbI_2 -rich condition.^[8] This phenomenon has been quickly applied to form homojunction in perovskite devices to enhance charge extraction or reduce charge recombination. Perovskite-perovskite homojunction was reported via adjusting the ratio of MAI and PbI_2 in double-layer MAPbI_3 films made by thermal evaporation.^[9] Similarly, a solution-processed n-type perovskite and thermally evaporated p-type perovskite bilayer were combined to form p–n homojunction structure, which was proposed to reduce carrier recombination by the enhanced built-in electric field and facilitated transport of charge carriers.^[10] Nevertheless, homojunction formed by self-doping may not be persistent under operation condition,^[11,12] considering the highly mobile ions in MHP, particularly under illumination.^[13] Molecular doping has been proven to be a feasible way for perovskites to alter their electronic properties and thus enhance device performance. For example, a p-type dopant of tetrafluorotetracyanoquinodimethane molecule was incorporated into perovskite

Dr. Q. Jiang, Dr. Z. Ni, Dr. G. Xu, Dr. Y. Lin, P. N. Rudd, Prof. J. Huang
Department of Applied Physical Sciences
University of North Carolina at Chapel Hill
Chapel Hill, NC 27599, USA
E-mail: jhuang@unc.edu

Dr. G. Xu, Dr. R. Xue, Prof. Y. W. Li, Prof. Y. F. Li
Laboratory of Advanced Optoelectronic Materials
College of Chemistry Chemical Engineering and Materials Science
Soochow University
Suzhou 215123, China
E-mail: ywli@suda.edu.cn

Prof. Y. Gao
Department of Physics and Astronomy
University of Rochester
Rochester, NY 14627, USA

 The ORCID identification number(s) for the author(s) of this article can be found under <https://doi.org/10.1002/adma.202001581>.

DOI: 10.1002/adma.202001581

precursor for blade coating, which caused a band bending in $\text{CH}_3\text{NH}_3\text{PbI}_3$ to match the work function of indium tin oxide (ITO) and realized the efficient hole-transport-layer-free PSCs.^[14] Later on, an oxidizing molybdenum tris(dithiolene) complex molecule was used to dope the perovskite surface, which enhanced the solar cell efficiency and achieved “tBP-free” device to enhance thermal stability.^[15]

In this study, we explore the feasibility of charge-transfer type molecule to selectively dope the perovskite surface using a material designed for hole conduction in perovskite solar cells. We synthesized a donor–acceptor symmetrical structure small molecule of 4,4',4'',4'''-(pyrazine-2,3,5,6-tetrayl) tetrakis (*N,N*-bis(4-methoxyphenyl) aniline) (PT-TPA), by incorporating an electron-deficient para-diazine as core and electron-donating methoxytriphenylamine as peripheral unit. The electron delocalization property of PT-TPA could induce an intermolecular charge transfer, and formed a stabilized resonance structure with a single electron in methoxy group, thus tending to accept an electron and dope perovskites. When coating PT-TPA on perovskite film, a p-type doping behavior was demonstrated to occur on the surface of perovskite material. The p-doped perovskite surface by PT-TPA small molecule forms a band bending which facilitates the hole extraction from perovskites into hole transport layer while reduces the electron-hole recombination at this interface.

As shown in **Figure 1a**, PT-TPA was synthesized by combining 2,3,5,6-tetrakis(4-bromophenyl) pyrazine and bis(4-methoxyphenyl) amine through a Buchwald–Hartwig reaction, delivering a yield as high as 72.3%. The detailed synthetic process and characterization (Figures S1 and S2, Supporting Information) were clearly described in Method section. As shown in **Figure 1b**, we used B3LYP/6-31G (d, p) based on density function theory (DFT) in the Gaussian 09 package to display the molecular geometry and the molecular orbitals of PT-TPA. 2,2',7,7'-tetrakis(*N,N*-dimethoxyphenylamine)-9,9'-spirobifluorenespirobifluorene (Spiro-OMeTAD) was also calculated for comparison (see details in **Figure S3** in the Supporting Information). First, according to the optimized molecular geometry, PT-TPA shows a more planar molecular configuration with the smaller dihedral angle (25.6°) than Spiro-OMeTAD. The flat geometry could be favorable for charge delocalization in the molecule. In order to display the electron distribution in PT-TPA, the highest occupied molecular orbitals (HOMO) and the lowest unoccupied molecular orbitals (LUMO) are also shown in **Figure 1b**. The HOMO of PT-TPA shows that the electron distribution is almost delocalized over the whole molecular skeleton due to the good π -conjugation character between the core and the auxiliary triphenylamine electron donors, but the electrons in Spiro-OMeTAD are barely delocalized in the whole molecule (**Figure S3**, Supporting Information). On the other hand, the LUMO of PT-TPA mainly distributes on the central core units and the LUMO energy level is −1.5 eV, which is lower than that of Spiro-OMeTAD (−1.0 eV). The lower LUMO for PT-TPA is easier to receive electron from the adjacent molecule. Moreover, we also calculated the enthalpy for PT-TPA to receive an electron. It releases 21.8 kcal mol^{−1} while the Spiro-OMeTAD just releases 7.5 kcal mol^{−1} after receiving an electron, which means that PT-TPA has better capability to receive an electron. We also calculated the electron excitation and electron transfer

process inside PT-TPA (**Figure S4**, Supporting Information). Therefore, we proposed that the delocalization effect may assist PT-TPA to form a resonance structure as illustrated in **Scheme 1**. First, under the driven of electron delocalization property, the electron of triphenylamine unit could be delocalized through π bridge, and formed radical cations around amino atom and radical anions in the para-diazine moiety. Then, one para-substituted methoxy group per radical triphenylamine offers resonance stabilization for charge and radicals in PT-TPA.^[16] An electron spin resonance (ESR) experiment on PT-TPA powders was conducted as shown in **Figure 1c**, wherein an ESR signal with a *g* value of 2.0025 can be clearly seen, suggesting radicals generated in the final stable structure. It is interesting to find that there is a single electron in methoxy group, which is likely to accept an electron from external environments. Therefore, we proposed that when PT-TPA contacting with perovskite material, the electron in perovskite could probably transfer to pair with the single electron of PT-TPA.

Moreover, the PT-TPA exhibited good thermal stability with a 5% weight-loss temperature at 430 °C by thermogravimetric analysis (TGA), as shown in **Figure 1d**. The HOMO level of PT-TPA was measured by the cyclic voltammetry. As shown in **Figure 1e**, PT-TPA displayed the first anodic wave at +0.59 eV versus Ag/AgCl in CH_2Cl_2 , 0.17 eV more positive than that of Spiro-OMeTAD (+0.42 eV). Considering that Spiro-OMeTAD has a HOMO level of −5.2 eV versus vacuum, the HOMO level of PT-TPA was thus determined to be −5.37 eV. The molecular structure of PT-TPA was characterized by ¹H and ¹³C NMR spectra (**Figures S1** and **S2**, Supporting Information).

We fabricated solar cells using the PT-TPA on perovskite surface in n–i–p structure solar cells with a device structure of glass/ITO/SnO₂/FA_xMA_{1−x}PbI₃/PT-TPA/Spiro-OMeTAD/Ag, as shown in **Figure 2a**. Here, SnO₂ and Spiro-OMeTAD are used as electron transport layer (ETL) and hole transport layer (HTL), respectively. The perovskite layer of FA_{0.92}MA_{0.08}PbI₃ was made by a typical two-step spin-coating method.^[4] The PT-TPA layer was also spin-coated on perovskite from solution of different concentration to control its thickness. A cross-sectional scanning electron microscopy (SEM) image of a completed device is shown in **Figure S5** in the Supporting Information. The PT-TPA layer is too thin to be distinguished in the cross-section SEM, because we used a low concentration PT-TPA of 1 mg mL^{−1} here. We made perovskite solar cells using different concentration of PT-TPA solution of 1, 5, and 10 mg mL^{−1}. And the corresponding thicknesses of PT-TPA layers are estimated as 4.7, 11.2, and 20.5 nm when they were deposited on smooth silicon substrates by measurement using ellipsometry. The devices achieved obvious PCE enhancement after introducing PT-TPA, and particularly the device open-circuit voltage (*V*_{OC}) was increased significantly. The champion device efficiency located in 1 mg mL^{−1} of PT-TPA condition (**Figure S6a** and **Table S1**, Supporting Information). We also measured the external quantum efficiency (EQE) of these devices. The corresponding integrated short current density (*J*_{SC}) of device with different concentrations of PT-TPA are almost similar, and the EQE of the device with PT-TPA is higher than the device without PT-TPA in the 725 to 800 nm range (**Figure S6b**, Supporting Information). SEM surface images of perovskite films in **Figure 2b,c** show that grain sizes of the perovskite films vary

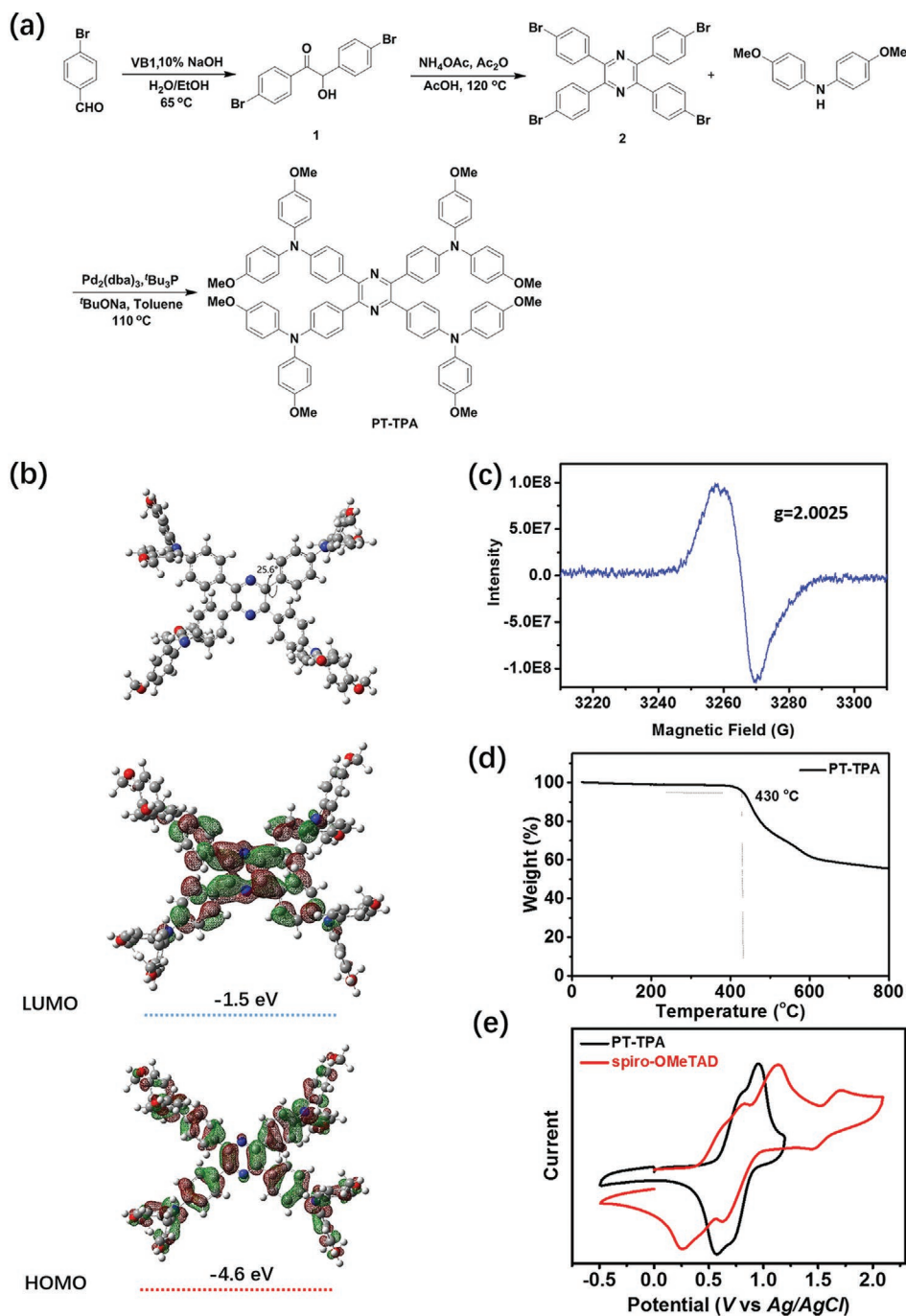
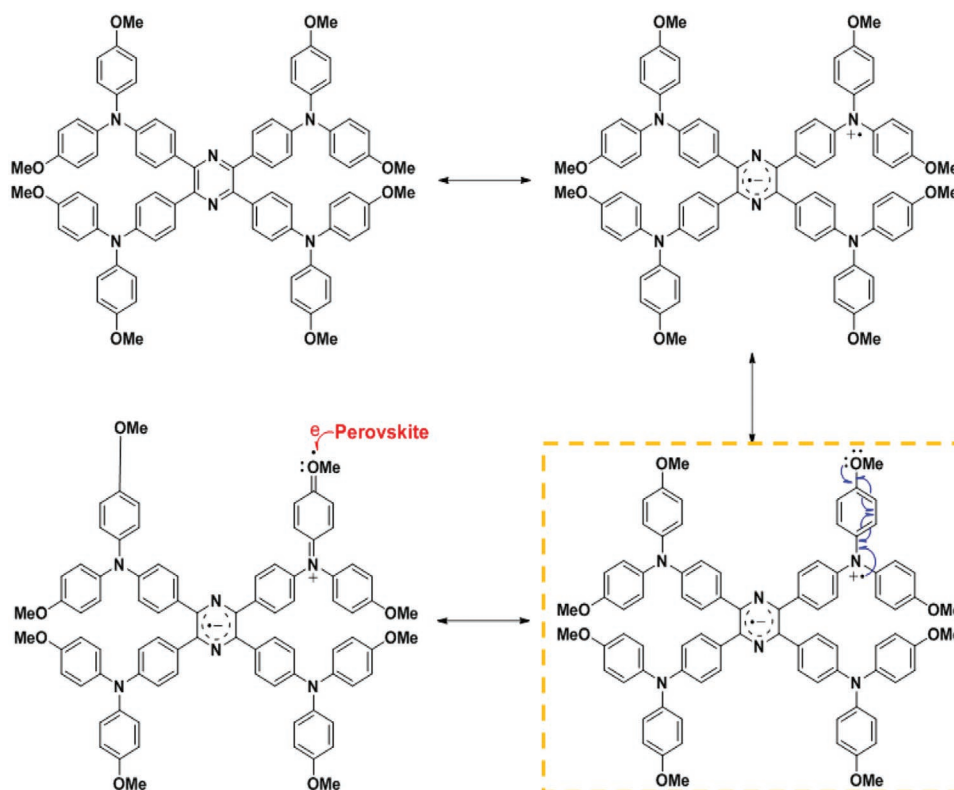


Figure 1. a) The synthetic route of PT-TPA is shown here, and the detailed synthetic process was described in the Experimental Section. PT-TPA was coupled with 2,3,5,6-tetrakis(4-bromophenyl) pyrazine (compound 2) and bis(4-methoxyphenyl) amine through a Buchwald–Hartwig reaction, delivering a 72.3% yield. Molecular structure of PT-TPA was characterized by ^1H and ^{13}C NMR spectra as shown in Figures S1 and S2 in the Supporting Information. b) Theoretical calculation with the DFT of PT-TPA: optimized molecular geometries (top). Frontier molecular orbital for LUMO (middle) and HOMO (bottom). c) ESR spectrum of PT-TPA evaporated powder measured at room temperature. d) Thermal stability test by thermogravimetric analysis (TGA) method. e) HOMO level calibration by cyclic voltammetry method. Compared with Spiro-OMeTAD, the HOMO level of PT-TPA was determined to be -5.73 eV.

from 300 to 1500 nm. PT-TPA modification slightly modified the topography of the films, while the grain structure remained intact.

The optimized concentration of PT-TPA for high efficiency devices is 1 mg mL^{-1} . The best-performing solar cell exhibited a high PCE of 23.4% in reverse scan condition, with a J_{SC} of



Scheme 1. Resonance structure of PT-TPA.

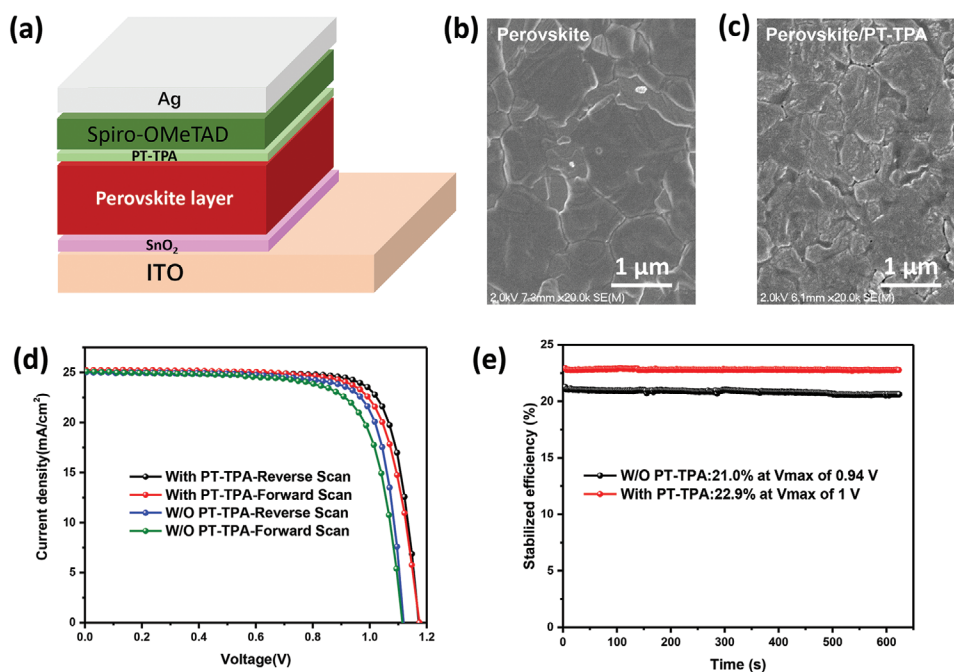


Figure 2. a) Architecture of n–i–p planar perovskite solar cells with structure: ITO/SnO₂/FA_{0.92}MA_{0.08}PbI₃/PT-TPA/Spiro-OMeTAD/Ag. b,c) SEM surface images of the pristine perovskite of FA_{0.92}MA_{0.08}PbI₃ and perovskite with PT-TPA. The PT-TPA layer is deposited by spin-coating a solution of 1 mg mL⁻¹ at 5000 rpm, and then annealed at 85 °C for 10 min. d) Current density–voltage (J – V) curves of the optimized devices without and with PT-TPA under reverse scan (1.2 to -0.1 V) and forward Scan (-0.1 to 1.2 V), testing under 1 Sun AM 1.5 simulated illumination. e) Efficiency evolution of the devices with and without PT-TPA under 1 Sun AM 1.5 simulated illumination for 10 min.

25.2 mA cm⁻², a V_{OC} of 1.17 V, and a fill factor (FF) of 79.3%, and a PCE of 22.6% under forward scan condition, with a J_{SC} of 25.2 mA cm⁻², a V_{OC} of 1.17 V, and an FF of 76.6%, as shown in Figure 2d. The control device without PT-TPA had a PCE of 21.9% under reverse scan condition, and a PCE of 20.5% on forward scan condition. Their photovoltaic performance parameters derived from these J - V curves are summarized in Table S2 (Supporting Information). The EQE of the champion device is shown in Figure S7 in the Supporting Information, which has an integrated J_{SC} of 24.0 mA cm⁻². Clearly the PCE enhancement by PT-TPA modification mainly comes from the V_{OC} increase from 1.12 to 1.17 V. The stabilized efficiency output of the devices without and with PT-TPA were measured and shown in Figure 2e. The best-performing device with PT-TPA showed a stabilized efficiency of 22.9%, while the device without PT-TPA showed a stabilized efficiency of 21.0%. To check the reproducibility of the device efficiency with PT-TPA, we collected the device efficiency of 45 devices from three batches (Figure S8, Supporting Information). The statistics of the PCE distribution confirmed the good reproducibility of our results. We also have tested the photostability of the devices without and with PT-TPA under 1 Sun illumination at about 65 °C for 550 h, and the results are shown in Figure S9 in the Supporting Information. Here we used a more thermally stable HTL of poly[bis(4-phenyl)(2,4,6-trimethylphenyl)amine] (PTAA) to replace Spiro-OMeTAD for stability testing.^[17] The initial efficiency of the cells is 20.55% and 19.42% under reverse scan direction, and the initial stabilized efficiency is 20.2% and 19.0% for the device with and without PT-TPA, respectively. Their J - V curves and the steady-state

efficiency results are presented in Figure S10 and Table S3 in the Supporting Information. The device with PT-TPA retained 88% of initial efficiency after 550 h testing, while the device without PT-TPA showed 85% of initial efficiency.

In order to get insights on the V_{OC} enhancement of devices with PT-TPA, we first conducted steady-state photoluminescence (PL) and time-resolved photoluminescence (TRPL) measurement of the perovskite films with or without PT-TPA to check whether PT-TPA passivates surface defects of perovskite films. Reduced non-radiative recombination due to passivation of surface defects by many types of passivation moieties has been broadly observed to enhance the V_{OC} of perovskite solar cells.^[3,4,18] Typical characteristics for successful defect passivation include higher PL intensity and longer TRPL lifetime because of the reduced non-radiative recombination sites in the perovskite films.^[19] We found that the PL intensity obviously reduced for the PT-TPA covered perovskite compared with the pristine perovskite film, as shown in Figure 3a. This was echoed by the significantly reduced TRPL lifetime from 1114 to 139 ns after PT-TPA modification, as shown in Figure 3b. This phenomenon is in striking contrast to general passivation techniques to enhance device V_{OC} . We also did PL and TRPL measurement to the perovskite samples with Spiro-OMeTAD while introducing the PT-TPA layer. As shown in Figure S11 (Supporting Information), the further reduced PL and shorter PL lifetime with addition of PT-TPA conclude that the PT-TPA helps charge transfer between the perovskite layer and Spiro-OMeTAD layer.

Since the quenching of PL either can be caused by the charge transfer of charges in excited states (photoinduced charge transfer) or at ground state (doping), we examined

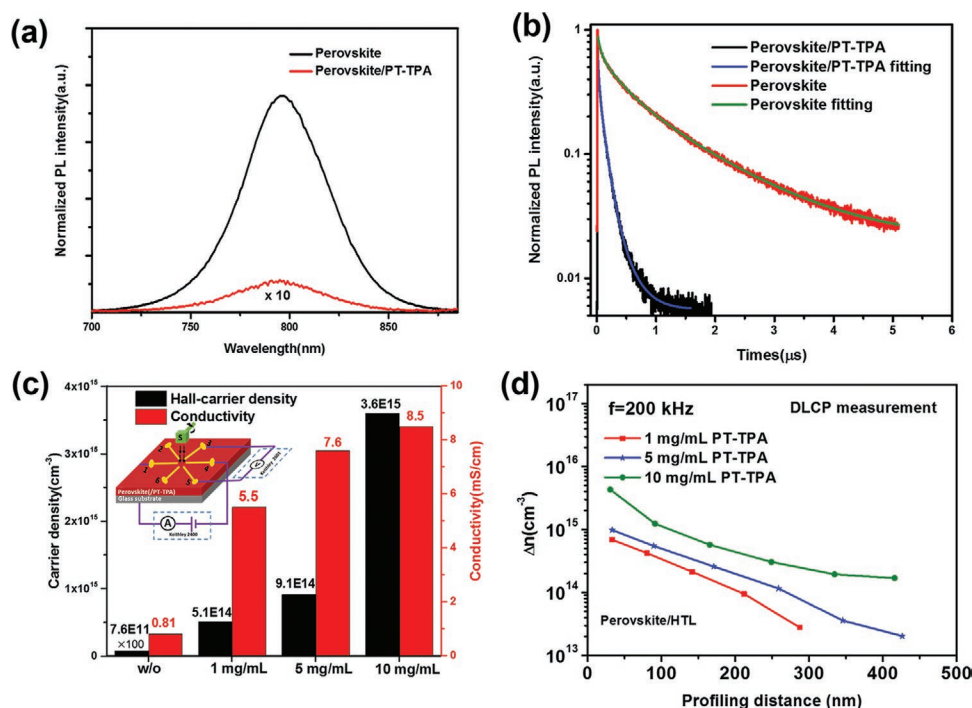


Figure 3. a) Photoluminescence (PL) spectra of FA_xMA_{1-x}PbI₃ films with (1 mg mL⁻¹, red) and without (black) PT-TPA. They are deposited on glass substrate. b) Time-resolved photoluminescence (TRPL) curves of FA_xMA_{1-x}PbI₃ perovskite with (1 mg mL⁻¹) (red) and without (black) PT-TPA. They are deposited on glass substrate. c) Charge carrier concentration by Hall effect measurement (black bar) and conductivity measurement (red bar) results of different perovskite films without and with PT-TPA, the inset shows the testing device geometry. d) Changed of doping carrier density in the perovskite layer measured by DLCP for perovskite solar cells with PT-TPA treatment from solution of different concentrations.

possible doping effect to perovskite by introducing PT-TPA to the surface. We measured the change of carrier concentration and the conductivity of the perovskite films by PT-TPA with a device geometry shown in inset of Figure 3c. For conductivity measurement, transmission line measurement was used to rule out the contact resistance. Hall measurement shows that all of the perovskite films are p-type. The pristine perovskite film has a hole concentration of $7.6 \times 10^{11} \text{ cm}^{-3}$, which is close to that measured by microwave conductivity method for MAPbI₃.^[20] After depositing PT-TPA on perovskite surface by spin-coating from solution with varied concentrations of 1, 5, and 10 mg mL⁻¹, the hole concentration of the perovskite films continuously increased to 5.1×10^{14} , 9.1×10^{14} , and $3.6 \times 10^{15} \text{ cm}^{-3}$, respectively. Here we assumed that doping occurred on the top few layers of perovskites according to simulation result shown below, which is around 8 nm. The carrier concentration increased by 671 times, and 4737 times when the perovskites were treated by PT-TPA with concentration of 1 and 10 mg mL⁻¹, respectively. Accordingly, the conductivity of the perovskite films also increased from 0.81 to 5.5, 7.6, and 8.5 mS cm⁻¹ with different PT-TPA concentration, which increased seven to ten times. The detailed conductivity testing results and calculated values are shown in Figure S12 and Table S4 (Supporting Information). The increase in conductivity is also an indication of a carrier density increase within the perovskite films. As a result, the increasing of hole concentration and conductivity in the films confirmed the obvious doping effect of PT-TPA on perovskite film and the doping type is p-type.

Since PT-TPA only contacted the surface of the perovskite, we expect only the top few layers of perovskite are doped. We further conducted drive-level capacitance profiling (DLCP) measurement to find out the carrier distributions in the perovskite film along the out of plane direction. DLCP is an established method to measure the carrier/trap distribution by scanning the depletion region through the devices and measure the charges being released using impedance spectroscopy.^[21] We have verified this method can be applied in perovskite solar cells.^[22] Figure S13 (Supporting Information) shows the location dependent carrier density in perovskite films from the perovskite/HTL interface to the perovskite/ETL interface. Here, a high AC frequency of 200 kHz was applied for the measurement to rule out the carrier contributions from the deep trap states. It is clear that the device with PT-TPA exhibits a higher carrier density near the perovskite/PT-TPA interface. The carrier density deep inside the perovskite film and perovskite/ETL interface barely changed. The measurement confirms that p-doping of the perovskite film by PT-TPA layer mainly occurs within the ~ 200 nm region from the perovskite/PT-TPA interface. We notice 200 nm is still much thicker than the thickness of PT-TPA/perovskite interface. This can be explained by the large roughness of the perovskite films and inhomogeneity of polycrystalline perovskites which results in a non-flat front of depletion edge. The carrier density of perovskite layer obtained from DLCP measurement in Figure S13 (Supporting Information) are different from Hall effect measurement, because the Hall effect measurement tells the free carrier density of a perovskite thin film, while the DLCP measures both the doping and trap densities of a perovskite film in a complete device. In order to get the carrier density increment after doping from

DLCP results, we can subtract the carrier density in perovskite w/o PT-TPA treatment from those with different solution concentration of PT-TPA. Figure 3d shows the results of changed doping carrier density distribution in the perovskite layer, and a clear exponential decay of carrier concentration from surface to the interior is observed. We derived average carrier densities of 3.05×10^{14} , 5.06×10^{14} , and $1.54 \times 10^{15} \text{ cm}^{-3}$ for perovskite films covered with PT-TPA processed from solution with concentrations of 1, 5, and 10 mg mL⁻¹, respectively. This is close to the Hall carrier concentration increase results of 5.09×10^{14} , 9.09×10^{14} , and $3.59 \times 10^{15} \text{ cm}^{-3}$ for the three types of samples.

We conducted X-ray photoelectron spectroscopy (XPS) measurement to find out the charge transfer between perovskite and PT-TPA. As shown in Figure 4a,b, the binding energy of Pb 4f core level and I 3d core level shifted to lower energy by 0.2 eV for perovskite/PT-TPA, indicating p-type doping of perovskites, because the core levels are closer to the Fermi level.^[23] A weak signal from Pb 4f_{7/2} at ~ 136.6 eV, which correspond to the metallic Pb⁰ state, was detected in the pristine perovskite without PT-TPA, while it disappeared in the perovskite with PT-TPA, we expected that the metallic lead was formed during XPS measurement, while the PT-TPA covering on perovskite surface can act as a buffer layer to prevent the formation of metallic Pb.

To simulate the interface interaction between the perovskite film and PT-TPA, first-principles calculation based on DFT was performed to understand the role of the small molecule doping mechanism. Figure 4c,d shows the iso-surfaces of the electron localization function (ELF) of the perovskite without and with PT-TPA. Clearly, the distributions of the ELF of the I atoms at the top of the perovskite become asymmetric and shift toward the PT-TPA molecule after contacting PT-TPA, indicating the attraction of the electron cloud of the I atoms by the PT-TPA molecule. To quantify the charge-transfer between perovskite and the PT-TPA molecule, we calculated the Hirshfeld charges of the Pb and I atoms in the perovskite without and with PT-TPA, as well as the charge changes of O, C, and H atom ($-\text{OCH}_3$, methoxy group) in the PT-TPA before and after depositing it on perovskite surface, as listed in Table S4 and Figure S14 in the Supporting Information. The average charge state of the I atoms on the vertices of the top octahedral structures increase from -0.07 to -0.03 after introducing PT-TPA. Those of the I and Pb atoms beneath the top layer are also increased by approximately 0.06 and 0.04 in perovskite/PT-TPA. Moreover, the charges of O atoms remain unchanged as -0.09 while the charges of C atoms in PT-TPA decrease from -0.03 to -0.06 , the charges of H atoms also show decrease. After combining the C, H, O atoms charges in $-\text{OCH}_3$ group, the methoxy group charge states change from 0.03 to -0.11 . Obviously, the methoxy group obtains electrons after PT-TPA depositing on perovskite surface. These changes clearly prove the electron transfer from perovskite to PT-TPA, which results in p-type doping of the perovskite surface. Meanwhile, it is noticed that the doping of the perovskite mainly happens in the top perovskite layers as the charge states of the I and Pb atoms in the second layer hardly change in perovskite/PT-TPA. Experimental observations and theoretical calculations both indicate that there is electron transfer from perovskite layer to PT-TPA molecules, and the schematic

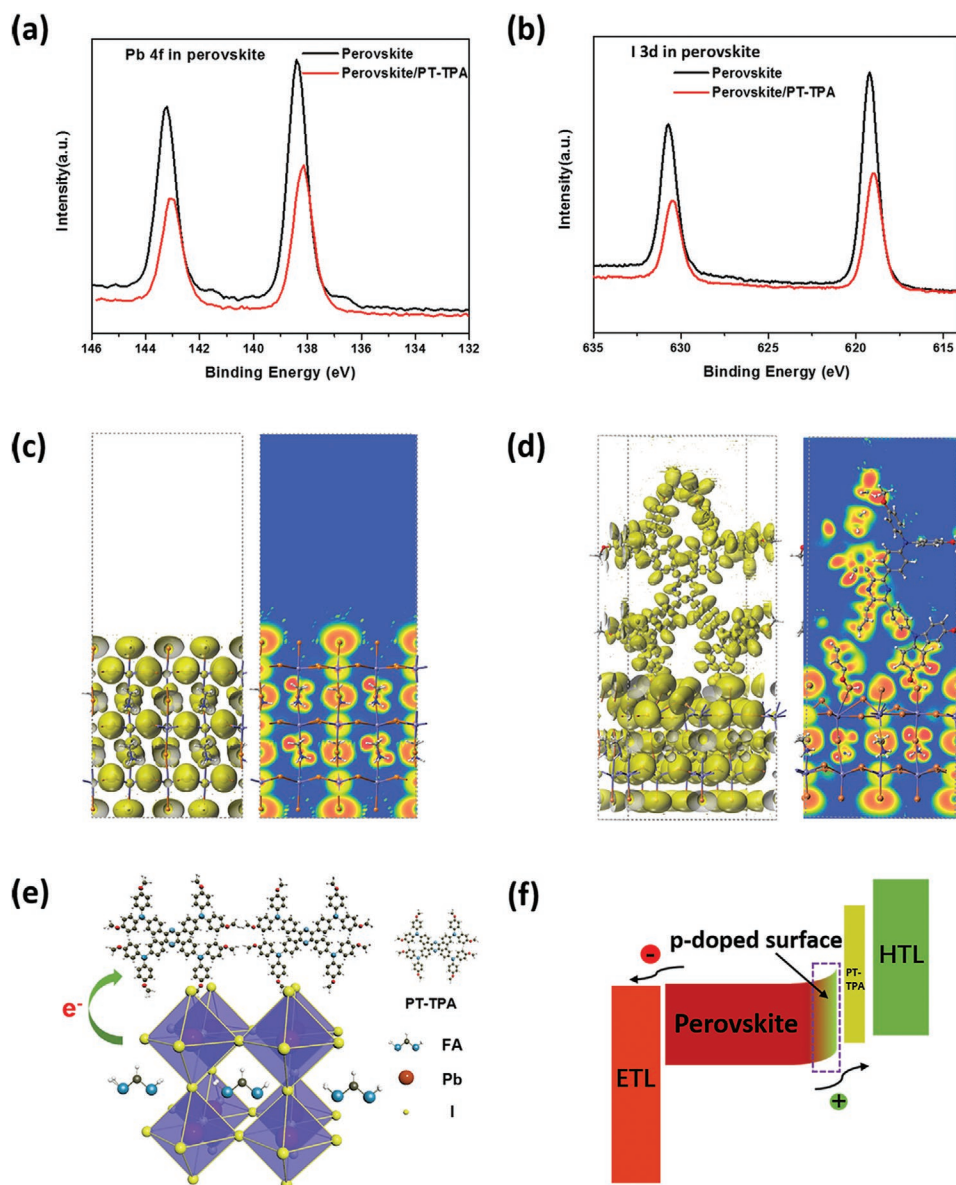


Figure 4. a) XPS results of Pb 4f core levels spectra of the pristine perovskite surface and perovskite/PT-TPA surface, b) XPS results of I 3d core levels spectra of the pristine perovskite surface and perovskite/PT-TPA surface. c) DFT calculation of the independent PT-TPA small molecule and perovskite itself. d) DFT calculation of the interaction between PT-TPA small molecule and perovskite. e) Schematic map of the electron-transfer from perovskite to PT-TPA. f) The band bending diagram at the perovskite surface due to the p-type doping by small molecule of PT-TPA.

illustration of electron transfer is shown in Figure 4e. The inter-molecular charge-transfer property and radical species can help PT-TPA to form a resonance structure, which makes PT-TPA to accept electrons from perovskite and thus p-dopes perovskite surface.

Finally, the p-doped perovskite surface by PT-TPA can affect the band structure of the perovskite and thus the band alignment at the interface of perovskite and HTL. Ultraviolet photoelectron spectroscopy (UPS) was studied to characterize the energy levels of $\text{FA}_{0.92}\text{MA}_{0.08}\text{PbI}_3$ perovskite before and after doping by PT-TPA of 1 mg mL^{-1} and also PT-TPA itself, the secondary electron cutoff edge and valence band spectra are shown in Figure S15 (Supporting Information). We derive a work

function of 4.30 eV for the perovskite material in this study, and a higher work function of 4.59 eV for PT-TPA. The result shows that perovskites have higher chemical potential than the small molecule of PT-TPA and thus turn to loss electrons to PT-TPA in ground states. In many cases, this work function difference may be compensated by the formation of dipole or formation of band bending due to doping. From the valence band spectra in Figure S15b (Supporting Information), the distance between valence band and Fermi level is much closer when perovskite is treated with 1 mg mL^{-1} of PT-TPA, showing that the energy band structure of perovskites indeed changed after they contact, which supports there is electron cloud wave function redistribution or charge transfer process. These results further support

that treating the perovskite surface with PT-TPA results in p-type doping to the perovskite surface. The optical band gap of $\text{FA}_{0.92}\text{MA}_{0.08}\text{PbI}_3$ perovskite is 1.53 eV from UV-vis absorption spectrum (Figure S16, Supporting Information), the derived diagram of band bending at the surface of perovskite due to p-type doping by PT-TPA is shown in Figure 4f. This band bending assists the extraction of photo generated holes to HTL and push electrons away from the perovskite/HTL interface, which should reduce the interface charge recombination and thus increase V_{OC} in the device. Indeed, the devices based on PT-TPA doped perovskite films have a higher V_{OC} of 1.17 V, 50 mV larger than the control devices without PT-TPA.

Finally, to understand the origin of the increased V_{OC} , we studied whether the homojunction formed between the p-doped perovskite surface and the nearly intrinsic perovskite underneath contributes to the enhanced device efficiency. Hence, we also used Solar Cell Capacitance Simulator (SCAPS) software to simulate the photocurrent curves of perovskite solar cells with and without the doping layer.^[24] We used the carrier concentration of perovskite layer derived from Hall-effect measurement and doping depth of ≈ 8 nm for simulation. We set the acceptor concentration of $7.6 \times 10^{11} \text{ cm}^{-3}$ in the whole perovskite thickness of 850 nm for the control device. And for the doping setting, acceptor concentration of $7.6 \times 10^{11} \text{ cm}^{-3}$ (842 nm, p)/ $5.1 \times 10^{14} \text{ cm}^{-3}$ (8 nm, p⁺) and $7.6 \times 10^{11} \text{ cm}^{-3}$ (842 nm, p)/ $3.6 \times 10^{15} \text{ cm}^{-3}$ (8 nm, p⁺) are used which correspond to the doping concentration in perovskites when they are covered by PT-TPA with concentration of 1 and 10 mg mL⁻¹. The simulated J - V curves and simulation parameters are shown in Figure S17 in the Supporting Information. The results show the homojunction formed does not contribute obviously to the enhanced efficiency here, which is consistent with a recent study.^[11]

We then examined other possible effect of surface doping of perovskites that may contributes to the enhanced V_{OC} . Here we characterized charge recombination lifetime in the devices by transient photovoltage measurement. The measurement was conducted with light bias of 1 Sun intensity to generate a carrier concentration comparable to operation condition, and a weak laser pulse was used to generate a small (<5%) modulation of V_{OC} . The decay time of photovoltage increased from 1.12 to 1.56 μs after introducing PT-TPA into perovskite devices (Figure S18, Supporting Information), indicating that the interfacial charge recombination is indeed slowed down because of the band bending induced faster hole extraction and repelling of electrons at the interface of perovskite and HTL.^[25] Hence, the enhanced device V_{OC} and efficiency should be mainly attributed to the p-doping-induced reducing recombination. To further verify this, we used SCAPS to simulate the influence of the reduced recombination on the device V_{OC} and PCE change. We varied the radiative recombination coefficient according to the measured recombination lifetime. As shown in simulation results summarized in Table 1, the calculated device V_{OC} and PCE agreed very well with our experiment results, which further supports the conclusion that enhanced device V_{OC} and PCE are caused by the reduced interfacial charge recombination.

In summary, a new strategy of molecule doping to the perovskite surface is introduced to develop high-efficiency perovskite solar cells. We successfully p-dope the surface of perovskite by

Table 1. The simulation results and experimental data on the influence of the reduced interfacial charge recombination on device V_{OC} and PCE.

	V_{OC} [V]	J_{SC} [mA cm ⁻²]	FF [%]	PCE [%]
Experiment-doped	1.17	25.2	79.3	23.4
Experiment-control	1.12	25.0	77.9	21.9
Simulation-doped	1.18	25.1	79.4	23.5
Simulation-control	1.13	25.1	77.9	22.0

depositing a small molecule of PT-TPA on perovskite surface, and it can form a band bending to assist charge separation at the interface and hole collection into hole transport layers. As a result, the resultant interfacial molecule doped perovskite device delivered an efficiency of 23.4% from photocurrent scanning and a stabilized efficiency of 22.9%. The concept of molecule doping exemplified here enables the controllable tailoring the band structure of perovskite-based materials that substantially improve the performance of optoelectronic devices.

Experimental Section

Materials: SnO_2 colloid precursor (tin(IV) oxide, 15% in H_2O colloidal dispersion) and lead iodine (PbI_2) were purchased from Alfa Aesar. Dimethylformamide (DMF), dimethyl sulfoxide (DMSO), and isopropanol (IPA) were purchased from Sigma-Aldrich. Formamidinium iodide (FAI) was from GreatCell Solar company. Methylammonium iodide (MAI) and methylammonium chloride (MACl) were purchased from Xi'an Polymer Light Technology in China. All of the purchased chemicals were used as received without further purification.

Synthesis Procedures of PT-TPA: Synthesis of PT-TPA proceeds as follows. The detailed synthetic process is shown in Figure 1a and the molecular structure of the small molecule was characterized by ¹H and ¹³C NMR spectra and MALDI-TOF mass spectrometry (Figures S1 and S2, Supporting Information).

1,2-bis(4-Bromophenyl)-2-hydroxyethanone (1): Vitamin B1 (5 g, 16.6 mmol), water (5 mL), and ethanol (EtOH) (100 mL) were added to a 250 mL round bottom flask. The system was cooled down below 0 °C with ice bath, then the pH was adjusted to 9–10 by adding 10% NaOH aqueous solution. After that, 4-bromobenzaldehyde (20 g, 108.1 mmol) was added and the mixture was stirred at 65 °C overnight. After cooling to room temperature, the solvent was evaporated and water (30 mL) was added to quench the reaction. Dichloromethane (DCM, 30 mL) was then added to extract the crude product three times. The organic phase was combined and dried with anhydrous magnesium sulfate (MgSO_4). After filtering MgSO_4 and evaporating solvent, the crude product was purified by silica gel chromatography using petroleum ether (PE)/DCM (3/1 v/v) as eluent to obtain the final product as white powder (3 g, 15%). ¹H NMR (300 MHz, CDCl_3) δ 7.76–7.73 (d, 2H), 7.57–7.54 (d, 2H), 7.48–7.45 (d, 2H), 7.20–7.17 (d, 2H), 5.87–5.85 (d, 1H), 4.47–4.45 (d, 1H). ¹³C NMR (150 MHz, CDCl_3) δ 197.59, 137.59, 132.38, 132.17, 131.92, 130.44, 129.51, 129.32, 122.94, 75.51.

2,3,5,6-Tetrakis(4-bromophenyl) pyrazine (2): (2.5 g, 6.76 mmol), ammonium acetate (1.56 g, 20.24 mmol), acetic anhydride (0.95 mL), and acetic acid (7.5 mL) were added to a 50 mL round bottom flask. The flask was evacuated and flushed with dry nitrogen three times. After heating at 120 °C for 3 h, the mixture was cooled down to room temperature. The filtered residue was washed by EtOH several times. Pale yellow powder was obtained (0.752 g, 31.8%). ¹H NMR (300 MHz, CDCl_3) δ 7.49 (s, 16H). ¹³C NMR (150 MHz, CDCl_3) δ 147.35, 136.63, 131.70, 131.29, 123.65.

4,4',4'',4'''-(Pyrazine-2,3,5,6-tetrayl) tetrakis (N,N-bis(4-methoxyphenyl) aniline) (PT-TPA) (3): (0.3 g, 0.43 mmol), bis(4-methoxyphenyl) amine (0.59 g, 2.58 mmol), $\text{Pd}_2(\text{dba})_3$ (78 mg, 85.2 μmol), and tBuONa (0.37 g,

3.85 mmol) were added to a 100 mL two-necked round bottom flask. The flask was evacuated and flushed with dry nitrogen three times. Then, a solution of tri-*tert*-butylphosphine in toluene (1 M, 170 μ L, 170 μ mol) and refined-anhydrous toluene (30 mL) were injected. The mixture was heated to 110 °C and stirred for 48 h. After cooling to room temperature, toluene was removed under reduced pressure. Water (30 mL) was further added, and DCM (30 mL) was then added to extract the crude product three times. The organic phase was combined and dried with anhydrous MgSO_4 . After filtration and solvent evaporation, the crude product was purified by silica gel chromatography using PE/DCM (3/1-1/1, v/v) as eluent to obtain the final product as yellow power (0.4 g, 72.3%). ^1H NMR (300 MHz, CDCl_3) δ 7.51–7.48 (d, 8H), 7.09–7.06 (d, 16H), 6.85–6.82 (d, 24H), 3.80 (s, 24H). ^{13}C NMR (150 MHz, CDCl_3) δ 155.99, 148.73, 146.32, 140.59, 130.55, 130.33, 126.87, 119.30, 114.66, 55.47. MS (MALDI-TOF): calcd for $\text{C}_{84}\text{H}_{72}\text{N}_6\text{O}_8$ [M] $^+$, 1293.51; found, 1293.605.

Perovskite Solar Cell Fabrication: A uniform and dense SnO_2 layer was deposited onto a ITO substrate by spin-coating SnO_2 nanoparticle solution (Alfa Aesar, tin(IV) oxide, 15% in H_2O colloidal dispersion, diluted by water into 2.67% concentration) at 4000 r.p.m. for 30 s, and annealed in ambient air at 150 °C for 30 min. After cleaning the SnO_2 substrate with ultraviolet ozone for 10 min to improve the surface wetting, 1.5 M of PbI_2 in DMF: DMSO (9:1) was spin-coated onto SnO_2 at 1500 r.p.m. for 30 s and then annealed at 70 °C for 1 min. After cooling to room temperature, a solution of FAI: MAI: MACI (90 mg:6.39 mg:9 mg in 1 mL IPA) was spin-coated onto the PbI_2 at 2000 r.p.m. for 30 s, followed by thermal annealing at 150 °C for 15 min in ambient air conditions (30–40% humidity). After perovskite formation, the samples were transferred to nitrogen atmosphere glove box for further processing. PT-TPA layer was deposited by spin-coating a solution of 1, 5, and 10 mg mL^{-1} which was dissolved in chlorobenzene at 5000 r.p.m. for 30 s and then annealed at 85 °C for 10 min. The Spiro-OMeTAD solution (72.3 mg Spiro-OMeTAD powder, 35 μ L Li-TFSI solution (bis(trifluoromethane) sulfonamide lithium salt) (260 mg mL^{-1} stock solution in acetonitrile), 30 μ L 4-*tert*-butylpyridine, all in 1 mL chlorobenzene) was spin-coated at 2000 r.p.m. for 30 s. For the stability test part, PTAA doped with 10% weight ratio of 4-Isopropyl-4'-methylidiphenyliodonium tetrakis(pentafluorophenyl)borate (TPFB) was used to replace Spiro-OMeTAD as hole transport layer. The concentration of PTAA is 30 mg mL^{-1} , and it is dissolved in toluene and the spin rate is 1500 r.p.m. for 30 s. Finally, the 120 nm metal electrode of silver film was thermally evaporated using a shadow mask of 0.08 cm^2 .

Characterizations and Measurements: *J*–*V* curves of the devices were measured using a source meter (Keithley 2400) under AM 1.5G simulated 1 Sun illumination (100 mW cm^{-2}) from the Newport xenon lamp. The light intensity was calibrated by a standard silicon cell with KG-5 filter. Steady-state power conversion efficiency was calculated by measuring stabilized photocurrent density under constant bias voltage (V_{max} point). The external quantum efficiency (EQE) spectra were measured by a lab-made setup of a Newport QE measurement kit by focusing a monochromatic light beam with wavelength from 300 to 900 nm onto the device. The morphologies and cross-section images were taken by a SEM Quanta 200 FEG environmental scanning electron microscope. The UPS and XPS data were collected by ESCAL AB 250Xi. The UPS employed HeI (21.22 eV) for excitation and the data were acquired at a bias of –10 V. The XPS spectra were calibrated using inorganic carbon at 284.8 eV. The PL and time-resolved PL spectrum were obtained by Micro-quantum FluoTime 300. The UV–vis spectra was obtained by Perkin Elmer UV–vis–NIR spectrophotometer Spectrum two. The Hall effect measurement was conducted with a six-contact van der Pauw method. The contacts were deposited by thermally evaporating 80 nm gold layers. Indium was used to attach the cooper wires on the gold contacts. The magnetic field was kept invariant as 0.2 T through the measurement. The Hall current was applied by a Keithley 2400 source meter and the Hall voltage was recorded by a Keithley 2601 source meter. The conductivity of the film was measured by using a transmission line measurement method to rule out the contact resistance. Gold electrodes with different channel lengths were thermally evaporated on perovskite films. The width of the channel is 500 μm , while the lengths of the channels are 400, 700, and 1200 μm .

Density Functional Theory (DFT) Simulation: For calculation of molecular geometry and the molecular orbitals of PT-TPA, the three-parameter hybrid B3LYP density functional method with the extended basis set 6-31+G (d, p) implemented in the GAUSSIAN 09 package was used. For calculation of doping mechanism, DFT calculations were performed by using the CASTEP package. The Perdew–Burke–Ernzerhof (PBE) correlation exchange functional at the GGA level and a plane wave basis set cutoff energy of 340 eV were adopted. A gamma-centered Monkhorst–Pack *k*-point grid of $3 \times 3 \times 1$ was adopted for each supercell. Geometry optimizations were carried out until the change in energy and the force on each atom are less than 1×10^{-5} eV per atom and 0.03 eV \AA^{-1} , respectively. After geometry optimizations, Hirshfeld charges were calculated with the cutoff distance for bond population set as 3.0 \AA . The lattice parameter of the perovskite supercell is $17.69 \times 17.69 \times 50$ \AA with a vacuum layer of 30 \AA between the top and the bottom perovskite layers.

Solar Cell Capacitance Simulator (SCAPS) Simulation: The simulation software of SCAPS (version 3.3.07) was used. An n–i–p planar structure of SnO_2 /perovskite/Spiro-OMeTAD was constructed for the solar cell simulations. The values of device and material parameters used in SCAPS are adopted from literatures and the experiment results of this work.^[11,24] And the main model parameters are summarized in Figure S14 and Table S5 (Supporting Information). The solar cells were simulated under global AM 1.5G solar spectrum and the operation temperature is 300 K.

Supporting Information

Supporting Information is available from the Wiley Online Library or from the author.

Acknowledgements

Q.J., Z.N., and G.X. contributed equally to this work. The authors acknowledge the financial support from Air Force Office of Scientific Research (AFOSR) (Grant No. A9550-16-1-0299) for the device work and support from the National Science Foundation under award DMR-1903981. The authors also thank the support from National Natural Science Foundation of China (Grant Nos. 51922074, 51673138) for the synthesis work of PT-TPA.

Conflict of Interest

The authors declare no conflict of interest.

Keywords

interfacial molecular doping, perovskite solar cells

Received: March 5, 2020

Revised: May 18, 2020

Published online:

- [1] a) H. Snaith, *Nat. Mater.* **2018**, 17, 372; b) J. Huang, Y. Yuan, Y. Shao, Y. Yan, *Nat. Rev. Mater.* **2017**, 2, 17042; c) A. Kojima, K. Teshima, Y. Shirai, T. Miyasaka, *J. Am. Chem. Soc.* **2009**, 131, 6050; d) M. A. Green, E. D. Dunlop, D. H. Levi, J. Hohl-Ebinger, M. Yoshita, A. Ho-Baillie, *Prog. Photovolt. Res. Appl.* **2019**, 27, 565; e) N. J. Jeon, J. H. Noh, W. S. Yang, Y. C. Kim, S. Ryu, J. Seo, S. I. Seok, *Nature* **2015**, 517, 476.
- [2] a) M. Saliba, T. Matsui, J.-Y. Seo, K. Domanski, J.-P. Correa-Baena, M. K. Nazeeruddin, S. M. Zakeeruddin, W. Tress, A. Abate,

- A. Hagfeldt, *Energy Environ. Sci.* **2016**, 9, 1989; b) N. J. Jeon, J. H. Noh, Y. C. Kim, W. S. Yang, S. Ryu, S. Il Seok, *Nat. Mater.* **2014**, 13, 897.
- [3] X. Zheng, B. Chen, J. Dai, Y. Fang, Y. Bai, Y. Lin, H. Wei, X. C. Zeng, J. Huang, *Nat. Energy* **2017**, 2, 17102.
- [4] Q. Jiang, Y. Zhao, X. Zhang, X. Yang, Y. Chen, Z. Chu, Q. Ye, X. Li, Z. Yin, J. You, *Nat. Photonics* **2019**, 13, 460.
- [5] a) F. Gao, Y. Zhao, X. Zhang, J. You, *Adv. Energy Mater.* **2019**, 9, 1902650; b) B. Chen, P. N. Rudd, S. Yang, Y. Yuan, J. Huang, *Chem. Soc. Rev.* **2019**, 48, 3842; c) T. Zhao, C.-C. Chueh, Q. Chen, A. Rajagopal, A. K.-Y. Jen, *ACS Energy Lett.* **2016**, 1, 757; d) I. L. Braly, D. W. deQuilettes, L. M. Pazos-Outón, S. Burke, M. E. Ziffer, D. S. Ginger, H. Hillhouse, **2018**, 12, 355.
- [6] T. Mishima, M. Taguchi, H. Sakata, E. Maruyama, S. Cells, *Sol. Energy Mater. Sol. Cells* **2011**, 95, 18.
- [7] W.-J. Yin, T. Shi, Y. Yan, *Appl. Phys. Lett.* **2014**, 104, 063903.
- [8] Q. Wang, Y. Shao, H. Xie, L. Lyu, X. Liu, Y. Gao, J. Huang, *Appl. Phys. Lett.* **2014**, 105, 163508.
- [9] B. Dänekamp, C. Müller, M. Sendner, P. P. Boix, M. Sessolo, R. Lovrincic, H. Bolink, *J. Phys. Chem. Lett.* **2018**, 9, 2770.
- [10] P. Cui, D. Wei, J. Ji, H. Huang, E. Jia, S. Dou, T. Wang, W. Wang, M. Li, *Nat. Energy* **2019**, 4, 150.
- [11] T. Kirchartz, D. Cahen, *eprint arXiv:1907.11218* **2019**, arXiv:1907.11218.
- [12] P. Calado, P. Barnes, *eprint arXiv:1905.11892* **2019**, arXiv:1905.11892.
- [13] a) G. Y. Kim, A. Senocrate, T.-Y. Yang, G. Gregori, M. Grätzel, J. Maier, *Nat. Mater.* **2018**, 17, 445; b) J. Xing, Q. Wang, Q. Dong, Y. Yuan, Y. Fang, J. Huang, *Phys. Chem. Chem. Phys.* **2016**, 18, 30484.
- [14] W.-Q. Wu, Q. Wang, Y. Fang, Y. Shao, S. Tang, Y. Deng, H. Lu, Y. Liu, T. Li, Z. Yang, A. Gruverman, J. Huang, *Nat. Commun.* **2018**, 9, 1625.
- [15] N. K. Noel, S. N. Habisreutinger, A. Pellaroque, F. Pulvirenti, B. Wenger, F. Zhang, Y.-H. Lin, O. G. Reid, J. Leisen, Y. Zhang, S. Barlow, S. R. Marder, A. Kahn, H. J. Snaith, C. B. Arnold, B. P. Rand, *Energy Environ. Sci.* **2019**, 12, 3063.
- [16] T. H. Schloemer, T. S. Gehan, J. A. Christians, D. G. Mitchell, A. Dixon, Z. Li, K. Zhu, J. J. Berry, J. M. Luther, A. Sellinger, *ACS Energy Lett.* **2019**, 4, 473.
- [17] L. Meng, C. Sun, R. Wang, W. Huang, Z. Zhao, P. Sun, T. Huang, J. Xue, J.-W. Lee, C. Zhu, *J. Am. Chem. Soc.* **2018**, 140, 17255.
- [18] S. Yang, J. Dai, Z. Yu, Y. Shao, Y. Zhou, X. Xiao, X. C. Zeng, J. Huang, *J. Am. Chem. Soc.* **2019**, 141, 5781.
- [19] a) N. K. Noel, A. Abate, S. D. Stranks, E. S. Parrott, V. M. Burlakov, A. Goriely, H. Snaith, *ACS Nano* **2014**, 8, 9815; b) D. W. DeQuilettes, S. Koch, S. Burke, R. K. Paranj, A. J. Shropshire, M. E. Ziffer, D. Ginger, *ACS Energy Lett.* **2016**, 1, 438.
- [20] Y. Bi, E. M. Hutter, Y. Fang, Q. Dong, J. Huang, T. Savenije, *J. Phys. Chem. Lett.* **2016**, 7, 923.
- [21] a) J. T. Heath, J. D. Cohen, W. Shafarman, *J. Appl. Phys.* **2004**, 95, 1000; b) C. Michelson, A. Gelatos, J. Cohen, *Appl. Phys. Lett.* **1985**, 47, 412.
- [22] Z. Ni, C. Bao, Y. Liu, Q. Jiang, W.-Q. Wu, S. Chen, X. Dai, B. Chen, B. Hartweg, Z. Yu, Z. Holman, J. Huang, *Science* **2020**, 367, 1352.
- [23] a) J. Lu, X. Lin, X. Jiao, T. Gengenbach, A. D. Scully, L. Jiang, B. Tan, J. Sun, B. Li, N. Pai, U. Bach, A. N. Simonov, Y.-B. Cheng, *Energy Environ. Sci.* **2018**, 11, 1880; b) D. Song, P. Cui, T. Wang, D. Wei, M. Li, F. Cao, X. Yue, P. Fu, Y. Li, Y. He, *J. Phys. Chem. C* **2015**, 119, 22812.
- [24] T. Minemoto, M. Murata, *J. Appl. Phys.* **2014**, 116, 054505.
- [25] a) Q. Jiang, L. Zhang, H. Wang, X. Yang, J. Meng, H. Liu, Z. Yin, J. Wu, X. Zhang, J. You, *Nat. Energy* **2016**, 2, 1; b) W. Chen, Y. Wu, Y. Yue, J. Liu, W. Zhang, X. Yang, H. Chen, E. Bi, I. Ashraful, M. Grätzel, L. Han, *Science* **2015**, 350, 944.